

# Inelastic Neutron Scattering and Magnetic Susceptibilities of the Single-Molecule Magnets $[\text{Mn}_4\text{O}_3\text{X}(\text{OAc})_3(\text{dbm})_3]$ ( $\text{X} = \text{Br}, \text{Cl}, \text{OAc}$ , and $\text{F}$ ): Variation of the Anisotropy along the Series

Hanspeter Andres,<sup>†</sup> Reto Basler,<sup>†</sup> Hans-Ulrich Güdel,<sup>\*,†</sup> Guillem Aromí,<sup>‡</sup> George Christou,<sup>‡</sup> Herma Büttner,<sup>§</sup> and Benoit Ruffé<sup>||</sup>

*Contribution from the Departement für Chemie und Biochemie, Universität Bern, Freiestrasse 3, 3000 Bern 9, Switzerland, Indiana University, Department of Chemistry, 800 East Kirkwood Avenue, Bloomington, Indiana 47405-7102, Institute Laue Langevin, Avenue des Martyrs, B. P. 156, F-38042 Grenoble Cedex 9, France, and Hahn-Meitner Institut, Glienicker Strasse 100, D-14109 Berlin-Wannsee, Deutschland*

Received March 16, 2000

**Abstract:** The single-molecule magnets (SMMs)  $[\text{Mn}_4\text{O}_3\text{X}(\text{OAc})_3(\text{dbm})_3]$  ( $\text{X} = \text{Br}, \text{Cl}, \text{OAc}$ , and  $\text{F}$ ) were investigated by a detailed inelastic neutron scattering (INS) study. Up to four magnetic excitations between the zero-field split levels of the lowest  $S = 9/2$  cluster ground-state have been resolved. From the determined energy-level diagrams and the relative INS intensities we can show that the inclusion of a rhombic term in the zero-field splitting (ZFS) Hamiltonian is essential in these compounds. On the basis of the Hamiltonian:  $\hat{H}_{\text{ZFS}} = D[\hat{S}_z^2 - 1/3S(S+1)] + E(\hat{S}_x^2 - \hat{S}_y^2) + B_4^0\hat{O}_4^0$ , the following sets of parameters are derived: For  $\text{X} = \text{Cl}$ :  $D = -0.529 \text{ cm}^{-1}$ ,  $|E| = 0.022 \text{ cm}^{-1}$ , and  $B_4^0 = -6.5 \times 10^{-5} \text{ cm}^{-1}$ ; for  $\text{X} = \text{Br}$ :  $D = -0.502 \text{ cm}^{-1}$ ,  $|E| = 0.017 \text{ cm}^{-1}$ , and  $B_4^0 = -5.1 \times 10^{-5} \text{ cm}^{-1}$ ; for  $\text{X} = \text{OAc}$ :  $D = -0.469 \text{ cm}^{-1}$ ,  $|E| = 0.017 \text{ cm}^{-1}$ , and  $B_4^0 = -7.9 \times 10^{-5} \text{ cm}^{-1}$ ; and for  $\text{X} = \text{F}$ :  $D = -0.379 \text{ cm}^{-1}$  and  $B_4^0 = -11.1 \times 10^{-5} \text{ cm}^{-1}$ . The wave functions derived from the energy analysis are in excellent agreement with the relative intensities of the observed INS transitions. The observed temperature maxima of the out-of-phase component of the variable frequency AC magnetic susceptibility  $T_{\max}[\chi'']$  correlate very well with the energy splittings determined by INS. Direct information about the rate of quantum tunneling is contained in the cluster wave functions derived in this study. The difference in the quantum tunneling between  $\text{X} = \text{Cl}$  and  $\text{Br}$  is shown to be directly related to differences in the rhombic anisotropy parameter  $|E|$ .

## Introduction

Magnetic particles of nanometer size have been of growing scientific interest in recent years.<sup>1,2</sup> On a small enough length scale the individual atomic spins cause their magnetic moments to align in the ordered pattern of a single domain, without the complication of domain walls separating regions of varying orientation. Thus, with a well-designed sample and experiment one can explore the range of mesoscopic magnetic phenomena, from the classical to the quantum limit.

Conventional nanomagnets have been obtained by sputtering, wet precipitation, or fragmentation of bulk ferro- and ferrimagnetic materials. For example, a scanning tunneling microscope served as a chemical-vapor deposition system to decompose  $\text{Fe}(\text{CO})_5$  and deposit the iron as arrays of almost identical, well-separated, roughly ellipsoidal magnets.<sup>3</sup> These approaches unfortunately suffer from the production of an ensemble of different-sized particles, whose response to an external perturbation such as a magnetic field is not uniform. An attempt to overcome this problems has been the use of the protein ferritin

as a substrate for the synthesis and the study of nanoscale magnetic particles.<sup>4</sup>

More recently, an exciting new alternative approach has been explored, as it has been discovered that certain polynuclear metal complexes can function as single domain nanomagnets at very low temperatures.<sup>5</sup> They have been termed single-molecule magnets (SMMs) or spin clusters.<sup>6</sup> Their advantage is that they are formed of identical particles, whose structures can be precisely determined from diffraction experiments. These molecular clusters are usually characterized by weak intermolecular exchange interactions in the  $0.01 \text{ cm}^{-1}$  range. This distinguishes the SMMs from the molecular-based magnets in a related active research area, in which extended exchange interactions are desired to induce a ferro- and antiferromagnetic order.

SMMs have been reported for a number of mixed valence  $\text{Mn(III)}-\text{Mn(IV)}$  clusters, such as the dodecanuclear complexes  $[\text{Mn}_{12}\text{O}_{12}(\text{O}_2\text{CR})_{16}(\text{H}_2\text{O})_x]$  ( $\text{R} = \text{Et}$ ,<sup>7</sup>  $x = 3$ ;  $\text{R} = \text{Me}$ <sup>8</sup> and  $\text{Ph}$ ,<sup>9</sup>  $x = 4$ ) and the series  $[\text{Mn}_4\text{O}_3\text{X}(\text{OAc})_3(\text{dbm})_3]$  ( $\text{dbm}^- =$  the

(4) Gider, S.; Awschalom, D. D.; Douglas, T.; Mann, S.; Charapala, M. *Science* **1995**, 268, 77.

(5) Gatteschi, D.; Caneschi, A.; Pardi, L.; Sessoli, R. *Science* **1994**, 265, 1054.

(6) Aubin, S. M.; Wemple, M. W.; Adams, D. M.; Tsai, H.-L.; Christou, G.; Hendrickson, D. N. *J. Am. Chem. Soc.* **1996**, 118, 7746.

(7) Epply, H. J.; Tsai, H.-L.; de Vries, N.; Folting, K.; Christou, G.; Hendrickson, D. N. *J. Am. Chem. Soc.* **1995**, 117, 301.

(8) Caneschi, A.; Gatteschi, D.; Sessoli, R.; Barra, A.-L.; Brunel, L.-C.; Guillot, M. *J. Am. Chem. Soc.* **1991**, 113, 5873.

<sup>†</sup> Universität Bern.  
<sup>‡</sup> Indiana University.  
<sup>§</sup> Institute Laue Langevin.  
<sup>||</sup> Hahn-Meitner Institut.

(1) Awschalom, D. D.; DiVincenzo, D. P.; Smyth, J. F. *Science* **1992**, 258, 414.  
(2) Awschalom, D. D.; DiVincenzo, D. P. *Phys. Today* **1995**, 48 (4), 43.  
(3) Kent, A. D.; Molnar, S.; Gider, S.; Awschalom, D. D. *J. Appl. Phys.* **1994**, 76, 6656.

anion of dibenzoylmethane) for various ligands X.<sup>6</sup> Also for the compounds  $[\text{Fe}_4(\text{OCH}_3)_6(\text{dpm})_6]$  ( $\text{dpm}^-$  = the anion of dipivaloylmethane),<sup>10</sup>  $[\text{Fe}_8\text{O}_2(\text{OH})_{12}(\text{tacn})_6]^{8+}$  (tacn = 1,4,7-triacacyclononane),<sup>11</sup> and  $[\text{V}_4\text{O}_2(\text{O}_2\text{CR})_7\text{L}_2]$  ( $\text{R} = \text{Et}$  and  $\text{Ph}$ ,  $\text{L} = 2,2'$ -bipyridine;  $\text{R} = \text{Et}$ ,  $\text{L} = 2$ -picoline)<sup>12</sup> single-molecule magnetic behavior has been reported.

SMMs are magnetizable units. In an external magnetic field their magnetic moments can be oriented either “up” or “down”, and when the external field is removed, the spins of the molecule will very slowly reorient at low enough temperatures. This is the case if the potential-energy barrier between the spin “up” and “down” states is significantly higher than  $kT$ . There are two requirements for this: A relatively large spin-ground-state  $S$ , and the axial zero-field splitting (ZFS) parameter  $D$  of the ground state must be large and negative. The height of the potential barrier is given by the product  $S^2 |D|$  for integer spin and  $(S^2 - 1/4)|D|$  for half-integer spin. Thus both high  $S$  and  $|D|$  values increase the barrier height.

With increasing  $S$ , dipolar interactions between neighboring clusters become more important and the typical SMM behavior may get lost. In a recently reported novel cyano-bridged  $\text{Mn}(\text{II})_9\text{Mo}(\text{V})_6$  cluster compound with a  $S = 5/2$  ground-state ferromagnetic intercluster interactions were shown to induce bulk magnetic order as high as  $T \approx 40 \text{ K}$ .<sup>13</sup>

Recently a  $S = 12$  ground state has been reported for the Mn(III) cluster  $[\text{Mn}_6\text{O}_4\text{X}_4]^{6+}$  ( $\text{X} = \text{Br}, \text{Cl}$ ), but due to a vanishing ZFS no SMM-type behavior was found.<sup>14</sup> The vanishing value of  $D$  in this cluster results from the high symmetry ( $T_d$ ) of the molecule, despite the large single-ion ZFS of the participating Jahn–Teller distorted Mn(III) ions. Thus the sign and size of  $D$  strongly depend on the geometric arrangement of the single-ion anisotropy axes with respect to the cluster symmetry, as the molecular ZFS is the vectorial addition of the single-ion ZFS.

In the title series  $[\text{Mn}_4\text{O}_3\text{X}(\text{OAc})_3(\text{dbm})_3]$  ( $\text{X} = \text{Br}, \text{Cl}, \text{OAc}$ , and F) the size of the ZFS is influenced by X as one introduces slightly different geometries of the central  $\text{Mn}(\text{III,IV})_4\text{O}_3\text{X}$  cubes.<sup>15,16</sup> The cluster contains one Mn(IV) and three Mn(III) ions arranged as shown in Figure 1a. The X ligand acts as a bridge between the three Mn(III) ions, and changing the chemical nature of X slightly changes the Mn-X bonding and thus the structure and the anisotropy. As seen in Figure 1a the cluster geometry is approximately trigonal. However, in the actual monoclinic ( $\text{X} = \text{Br}, \text{Cl}$ , and OAc) and triclinic ( $\text{X} = \text{F}$ ) crystal structures it is slightly distorted. Previously these complexes were reported to have a well-isolated  $S = 9/2$  ground state that is split by the axial ZFS parameter  $D$ .<sup>6,15</sup> Variable-field magnetic susceptibility data have been collected for these distorted cubane complexes. Least-squares fits of these magnetic data revealed two local minima for  $D > 0$  and  $D < 0$ . The fits

(9) Sessoli, R.; Tsai, H.-L.; Schake, A. R.; Wang, S.; Vincent, J. B.; Folting, K.; Gatteschi, K.; Gatteschi, D.; Christou, G.; Hendrickson, D. N. *J. Am. Chem. Soc.* **1993**, *115*, 1804.

(10) Barra, A. L.; Caneschi, A.; Cornia, A.; de Bianca, F. F.; Gatteschi, D.; Sangregorio, C.; Sessoli, R.; Sorace, I. *J. Am. Chem. Soc.* **1999**, *121*, 5302.

(11) Sangregorio, C.; Ohm, T.; Paulsen, C.; Sessoli, R.; Gatteschi, D. *Phys. Rev. Lett.* **1997**, *78*, 4645.

(12) Castro, S. L.; Sun, Z.; Grant, C. M.; Bollinger, J. C.; Hendrickson, D. N.; Christou, G. *J. Am. Chem. Soc.* **1998**, *120*, 2365.

(13) Larionova, J.; Gross, M.; Pilkington, M.; Andres, H.; Stoeckli-Evans, E.; Güdel, H. U.; Decurtins, S. *Angew. Chem.* **2000**, in press.

(14) Aromi, G.; Knapp, M. J.; Claude, J.-P.; Huffman, J. C.; Hendrickson, D. N.; Christou, G. *J. Am. Chem. Soc.* **1999**, *121*, 5489.

(15) Wang, S.; Tsai, H.-L.; Libby, E.; Folting, K.; Streib, W. E.; Hendrickson, D. N.; Christou, G. *Inorg. Chem.* **1996**, *35*, 7578.

(16) Wemple, M. W.; Adams, D. M.; Folting, K.; Hendrickson, D. N.; Christou, G. *J. Am. Chem. Soc.* **1995**, *117*, 7275.

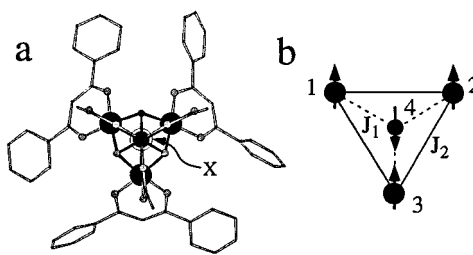


**Figure 1.** (a) The structure of  $[\text{Mn}_4\text{O}_3\text{X}(\text{OAc})_3(\text{dbm})_3]$  ( $\text{X} = \text{Br}, \text{Cl}$ ,  $\text{OAc}$ , and F) viewed along the pseudo- $C_3$  axis. The Mn ions are shown in black with larger spheres for the Mn(III) ions. (b) Schematic representation of the exchange coupling in the title compounds with the principal exchange pathways  $J_1$  and  $J_2$ .

with  $D < 0$  gave  $D$  values in the range  $-0.29$  to  $-0.35 \text{ cm}^{-1}$ , whereas the fits with  $D > 0$  gave  $D$  values in the range  $0.43$ – $0.55 \text{ cm}^{-1}$ . From the X-ray structures the authors in ref 6 conclude that  $D$  is most likely negative for these complexes. For  $\text{X} = \text{Cl}$  this has been confirmed by a high-field high-frequency EPR study where the data were successfully explained with an axial ZFS parameter  $D = -0.53 \text{ cm}^{-1}$  supplemented by a quartic ZFS parameter  $B_4^0 = -7.3 \times 10^{-5} \text{ cm}^{-1}$ .<sup>17</sup> For the remaining ligands X no additional information on the ZFS is available, but is desired for a thorough study of the influence of X on the ZFS.

As the compounds  $[\text{Mn}_4\text{O}_3\text{X}(\text{OAc})_3(\text{dbm})_3]$  ( $\text{X} = \text{Br}, \text{Cl}$ ,  $\text{OAc}$ , and F) are relatively easily prepared in big amounts they are attractive for the study of the zero-field split levels of the cluster-ground state as a function of X by inelastic neutron scattering (INS). This method is a very powerful tool to investigate spin excitations in polynuclear transition and rare-earth metal clusters.<sup>18,19</sup> Being a spectroscopic method it provides direct access to the energy splittings resulting from exchange and anisotropy interactions. In contrast to EPR, it is a zero-field experiment, which requires no assumption about the Landé factor  $g$ . INS has been used to measure exchange and anisotropy splittings in numerous clusters and recently to determine the ZFS in the SMMs  $[\text{Fe}_8\text{O}_2(\text{OH})_{12}(\text{tacn})_6]^{20}$  and  $[\text{Mn}_{12}\text{O}_{12}(\text{OAc})_{16}(\text{H}_2\text{O})_4]$ .<sup>21,22</sup> The derived ZFS parameters of the  $S = 10$  ground states in these two compounds, in particular the transverse terms, provide crucial information for the interpretation of their macroscopic quantum tunneling behavior.

In this report we present a detailed INS study of the four title complexes with cold neutrons at the Institute Laue Langevin (ILL) in Grenoble and the Hahn-Meitner Institute (HMI) in Berlin. The high-resolution measurements enabled the resolution of all four allowed inelastic transitions within the ground states of  $[\text{Mn}_4\text{O}_3\text{X}(\text{OAc})_3(\text{dbm})_3]$  ( $\text{X} = \text{Br}, \text{Cl}$ , and OAc) and the resolution of three inelastic features for  $[\text{Mn}_4\text{O}_3\text{F}(\text{OAc})_3(\text{dbm})_3]$ . From the experimentally determined energy-level diagrams we deduce the relevant ZFS parameters. The derived axial ZFS

(17) Aubin, S. M.; Dilley, N. R.; Pardi, L.; Krzystek, J.; Wemple, M. W.; Brunel, L.-B.; Maple, M. B.; Christou, G.; Hendrickson, D. N. *J. Am. Chem. Soc.* **1998**, *120*, 4991.

(18) Güdel, H. U. In *Molecular Magnetism: From Molecular Assemblies to Devices*; Coronado, E., Delhás, P., Gatteschi, D., Miller, J. S., Eds.; NATO Advanced Study Institute Series E 321; Kluwer Academic Publishers: Dordrecht, 1996; pp 229–242.

(19) Andres, H.; Decurtins, S.; Güdel, H. U. In *Frontiers of Neutron Scattering*; Furrer, A., Ed.; Proceedings of the Seventh Summer School on Neutron Scattering; World Scientific: Singapore, 2000; pp 149–167.

(20) Carciuffo, R.; Amoretti, G.; Murani, A.; Sessoli, R.; Caneschi, A.; Gatteschi, D. *Phys. Rev. Lett.* **1998**, *81*, 4744.

(21) Hennion, M.; Pardi, L.; Mirebeau, I.; Suard, E.; Sessoli, R.; Caneschi, A. *Phys. Rev. B* **1997**, *56*, 8819.

(22) Mirebeau, I.; Hennion, M.; Casalata, H.; Andres, H.; Güdel, H. U.; Irodova, A. V.; Caneschi, A. *Phys. Rev. Lett.* **1999**, *83*, 628.

parameters  $D$  nicely reproduce the observed trends in the temperature maxima of the out-of-phase alternating field (AC) magnetic susceptibility data.<sup>6,17</sup> These out-of-phase AC data are a direct measure of the potential-energy barrier between the spin “up” and “down” states.

In addition, from the determined energy-level diagrams and from the relative INS intensities we can show that the inclusion of a transverse rhombic anisotropy term in the ZFS Hamiltonian is essential in these compounds. This term critically influences the composition of the cluster wave functions. This information on the wave functions will help to develop a quantitative understanding of the quantum tunneling of the magnetization observed for  $[Mn_4O_3Cl(OAc)_3(dbm)_3]$ , where for  $T < 0.6$  K a temperature independent relaxation rate of  $3.2 \times 10^{-2}$  s $^{-1}$  has been determined.<sup>17</sup>

## Experimental Section

**Synthesis and Characterization.** The compounds  $[Mn_4O_3X(OAc)_3(dbm)_3] \cdot nCH_2Cl_2$  ( $X = Br, Cl, OAc$ , and  $F$ ) were synthesized as described in ref 23. The compound  $[Mn_4O_3F(OAc)_3(dbm)_3] \cdot nCH_2Cl_2$  was prepared in two different batches, either by immediate or slow precipitation from the reaction solution, referred to as batch F1 and F2, respectively. All compounds were dried in air.

All compounds were characterized by elemental analysis, infrared spectroscopy, nuclear magnetic resonance and X-ray powder diffraction using the program LAZY PULVERIX<sup>24</sup> and the structural data given in refs 15 and 16. From the comparison of the experimental and calculated X-ray powder diffraction diagrams we conclude the following. The sample  $[Mn_4O_3OAc(OAc)_3(dbm)_3]$  is single phase, whereas the samples  $[Mn_4O_3X(OAc)_3(dbm)_3]$  ( $X = Br$  and  $Cl$ ) contain an impurity phase of  $\sim 5\text{--}10\%$ . In contrast to magnetic measurements the INS technique is not susceptible to such impurities. The powder X-ray diffraction diagrams of the two batches F1 and F2 are different and have no similarity with the calculated pattern from ref 16. Both batches consist of more than one phase. The pattern of batch F1 is contained in the pattern of batch F2. Loss or partial loss of the  $CH_2Cl_2$  solvent molecules is likely responsible for this complication; the neutrons thus probe tetrานuclear  $[Mn_4O_3F(OAc)_3(dbm)_3]$  complexes with slightly different environments.

Approximately 8 g of each polycrystalline sample  $[Mn_4O_3X(OAc)_3(dbm)_3]$  ( $X = Br, Cl, OAc$ , and  $F$ ) were sealed under helium in an aluminum container of 15 mm diameter and 55 mm length suitable for INS experiments.

**Physical Measurements.** INS spectra were recorded on the time-of-flight instruments V3 at the HMI (Berlin) and IN5 at the ILL (Grenoble) using cold neutrons with an incident neutron wavelength of 5.5 Å and 7.5 Å, respectively, at  $T = 1.8, 3.0, 6.0$  and 18 K.

The data treatment involved the subtraction of a background spectrum using an empty aluminum container of the same size and the calibration of the detectors by means of a spectrum of vanadium metal. The time-of-flight to energy conversion and the data reduction were done with the standard program INX at both HMI and ILL. Further data treatment was done using the commercial program Igor-Pro 3.14 (Wave Metrics).

Alternating current magnetic susceptibility measurements in the temperature range 1.8–3.8 K were carried out on a Quantum Design MPMS-XL SQUID magnetometer. The data were corrected for the diamagnetic contribution, which was estimated from Pascal’s constants.

## Results

In Figure 2 the INS spectra (solid lines) of a polycrystalline sample of  $[Mn_4O_3OAc(OAc)_3(dbm)_3]$  are shown for the temperatures  $T = 1.8, 3.0, 6.0$ , and 18.0 K, respectively. The spectra were recorded with an incident neutron wavelength of  $\lambda_i = 7.5$  Å and are depicted in the energy-transfer range  $-5.25\text{--}5.25$  cm $^{-1}$  with positive values for neutron-energy loss. The resolution is 0.261 cm $^{-1}$  at zero-energy transfer.

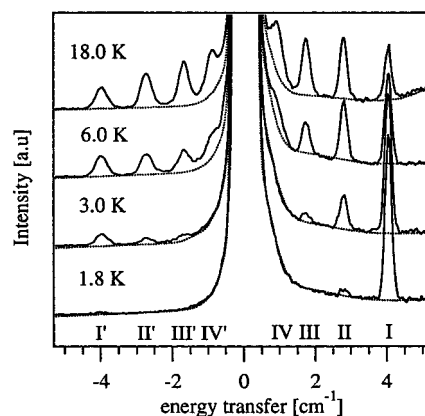


**Figure 2.** INS spectra (full lines) of a polycrystalline sample of  $[Mn_4O_3OAc(OAc)_3(dbm)_3]$  recorded on IN5 at  $\lambda_i = 7.5$  Å for temperatures  $T = 1.8, 3.0, 6.0$ , and 18 K, respectively. The peaks are labeled at the bottom of the Figure. The dotted lines represent a convolution of the experimental background with the quasi-elastic and elastic peak features.

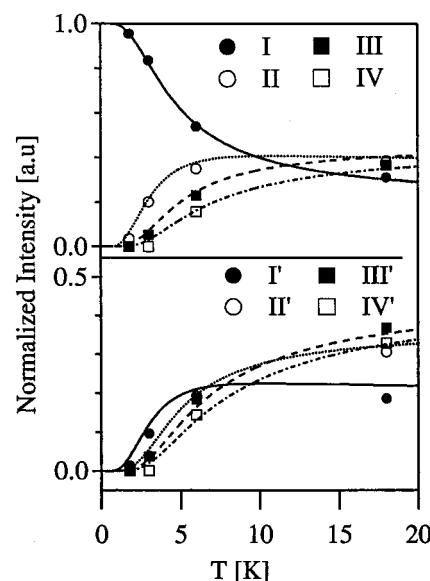


**Figure 3.** Scattering intensities of the transitions in Figure 2 as a function of temperature. The data were scaled to the normalized intensity of transition I at  $T = 1.8$  K. The solid, dotted, dashed, and dash-dotted lines are the calculated intensities of the transitions I–IV and I'–IV', respectively.

At 1.8 K we observe a prominent inelastic peak **I** at 4.013(4) cm $^{-1}$ . An increase of the temperature to 3.0, 6.0, and 18.0 K is concomitant with the appearance of three hot transitions **II**, **III**, and **IV** at 2.762(5), 1.714(5), and 0.937(5) cm $^{-1}$ , respectively. On the neutron energy gain side in Figure 2 these four transitions are also observed at elevated temperatures and are labeled **I'**–**IV'**. The problem of quasi-elastic scattering due to the hydrogen atoms is inherent in the INS spectra of Figure 2 and manifests itself in a broad temperature dependent shoulder of the elastic peak on the neutron-energy loss side between 0 and 1.5 cm $^{-1}$ .

The INS intensities resulting from least-squares fits with Gaussian line shapes and the depicted backgrounds in Figure 2 (dotted lines) are shown as a function of the temperature  $T$  in Figure 3.

In Figure 4 the INS spectra for the polycrystalline samples  $[Mn_4O_3X(OAc)_3(dbm)_3]$  ( $X = Br, Cl, OAc$ , and  $F$ ) are depicted as full circles with experimental errors. The spectra were recorded with an incident neutron wavelength  $\lambda_i$  of 7.5 Å and a temperature  $T = 18$  K. The INS spectra of  $[Mn_4O_3Br(OAc)_3]$

(23) Guillem, A.; Christou, G. Manuscript in preparation.

(24) Yvon, K.; Jeitschko W.; Parthé, E. *J. Appl. Crystallogr.* **1977**, *10*, 73.

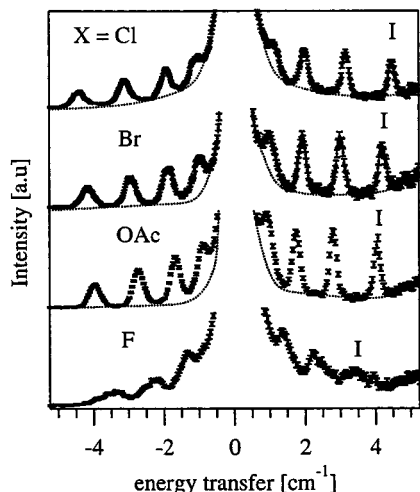


**Figure 4.** INS spectra for polycrystalline samples of  $[\text{Mn}_4\text{O}_3\text{X}(\text{OAc})_3(\text{dbm})_3]$  ( $\text{X} = \text{Br}, \text{Cl}, \text{OAc}$ , and  $\text{F}$ ) recorded on IN5 at  $\lambda_i = 7.5 \text{ \AA}$  for a temperature  $T = 18 \text{ K}$ . The backgrounds are included as dotted lines for  $\text{X} = \text{Cl}, \text{Br}$  and  $\text{OAc}$  and transition **I** is labeled.

**Table 1.** Experimental and Calculated Transition Energies **I**–**IV** Using Eq 4 with the Parameters in Table 4 for  $[\text{Mn}_4\text{O}_3\text{X}(\text{OAc})_3(\text{dbm})_3]$  ( $\text{X} = \text{Br}, \text{Cl}, \text{OAc}$ , and  $\text{F}$ )<sup>a</sup>

label	energy [cm <sup>-1</sup> ]							
	$\text{X} = \text{Cl}$		$\text{X} = \text{Br}$		$\text{X} = \text{OAc}$		$\text{X} = \text{F}$	
	exp	calc		exp	calc		exp	calc
I	4.439(3)	4.441	4.185(3)	4.184	4.013(4)	4.013	3.41(4)	3.408
II	3.139(2)	3.134	2.979(3)	2.986	2.762(5)	2.802	2.23(4)	2.238
III	1.962(2)	1.963	1.902(2)	1.898	1.714(5)	1.770	1.33(4)	1.331
IV	1.126(4)	1.127	1.033(4)	1.033	0.937(5)	0.855	-	0.619

<sup>a</sup> The experimental errors are given in brackets.

(dbm)<sub>3</sub>] and  $[\text{Mn}_4\text{O}_3\text{Cl}(\text{OAc})_3(\text{dbm})_3]$  are very similar to the INS spectrum of  $[\text{Mn}_4\text{O}_3\text{OAc}(\text{OAc})_3(\text{dbm})_3]$  with four nicely resolved inelastic transitions on both sides of the energy-transfer spectrum. The resulting transition energies from least-squares fits assuming Gaussian line shapes and the depicted backgrounds (dotted lines) in Figure 4 are listed in Table 1. For  $[\text{Mn}_4\text{O}_3\text{F}(\text{OAc})_3(\text{dbm})_3]$ , the features are much broader and only three maxima can be determined, which are included in Table 1. In Figure 4 the position of transition **I** is indicated for the four compounds and we observe a decrease of its energy along the series  $\text{X} = \text{Cl}, \text{Br}, \text{OAc}$ , and  $\text{F}$  of about 25%. The same trend is observed for the other inelastic transitions **II**–**IV** as seen by an inspection of Figure 4 and Table 1.

In Figure 5 the INS spectra for the two batches F1 and F2 of  $[\text{Mn}_4\text{O}_3\text{F}(\text{OAc})_3(\text{dbm})_3]$  are shown in the spectral region of transition **I** ( $2.4$ – $4.5 \text{ cm}^{-1}$ ). The spectra were recorded with an incident neutron wavelength  $\lambda_i$  of  $7.5 \text{ \AA}$  and a temperature  $T = 1.8 \text{ K}$ . Analogous to  $[\text{Mn}_4\text{O}_3\text{OAc}(\text{OAc})_3(\text{dbm})_3]$  we would expect at this temperature a single cold transition **I** in this energy-transfer range. The bands in Figure 5 are clearly superpositions of several components. The spectra of batches F1 and F2 can be decomposed by Gaussian deconvolution into three and four components, respectively. They are labeled  $\mathbf{I}_a$ – $\mathbf{I}_d$  in Figure 5. Thus the samples F1 and F2 contain at least 3 and 4 clusters with slightly different ground-state properties, respectively.

From the  $1.8 \text{ K}$  INS spectra of  $[\text{Mn}_4\text{O}_3\text{X}(\text{OAc})_3(\text{dbm})_3]$  ( $\text{X} = \text{Cl}, \text{Br}$ , and  $\text{OAc}$ ) we have determined the dependence of the INS intensity of transition **I** on  $Q$ , the length of the scattering vector  $\vec{Q}$ . In Figure 6 the IN5 and V3 data are combined with full and open circles, respectively. With the incident neutron

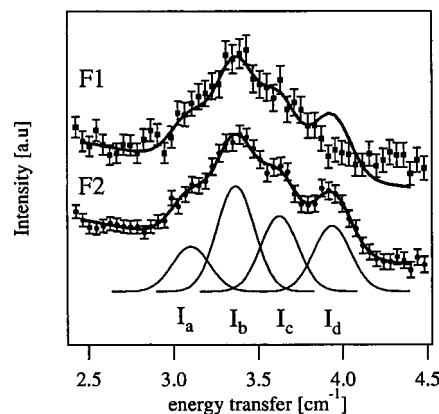


**Figure 5.** INS spectra for  $[\text{Mn}_4\text{O}_3\text{F}(\text{OAc})_3(\text{dbm})_3]$  recorded on IN5 at  $\lambda_i = 7.5 \text{ \AA}$  and a temperature  $T = 1.8 \text{ K}$ . The spectral region of transition **I** is depicted for the two different batches F1 and F2, respectively. A simulation with the depicted four Gaussians  $\mathbf{I}_a$ – $\mathbf{I}_d$  is included as a solid line in both spectra.

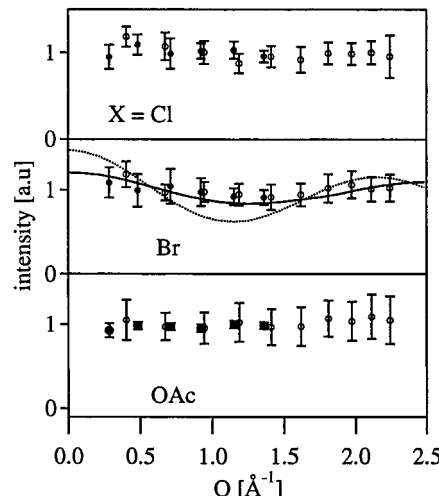


**Figure 6.** Experimental  $Q$  dependencies with errors ( $3\sigma$ ) of the INS intensity of transition **I** for  $[\text{Mn}_4\text{O}_3\text{X}(\text{OAc})_3(\text{dbm})_3]$  ( $\text{X} = \text{Br}, \text{Cl}$ , and  $\text{OAc}$ ) are depicted with full and open circles for the IN5 and V3 data, respectively. The dotted and solid line represent the calculated curves (eq 6) for a distinct  $Q$  and the range  $Q \pm 0.5 \text{ \AA}^{-1}$  for  $\text{X} = \text{Br}$ , respectively. The form factors  $F_i(Q)$  and the Mn–Mn distances  $R_{ij}$  in the relevant calculations are taken from the literature.<sup>15,16,33</sup>

wavelength  $\lambda_i$  of  $7.5 \text{ \AA}$  on IN5 we cover the  $Q$ -range  $0.2$ – $1.5 \text{ \AA}^{-1}$ , whereas with  $\lambda_i = 5.5 \text{ \AA}$  on V3 we access the broader  $Q$ -range from  $0.3$  to  $2.3 \text{ \AA}^{-1}$ . The two data sets agree within the plotted errors of  $3\sigma$ . None of the three compounds exhibits a pronounced  $Q$  dependence of the INS intensity in the  $Q$ -range  $0.2$  to  $2.3 \text{ \AA}^{-1}$ , and the behavior of the three compounds is very similar. The experimental behavior is clearly indicative for magnetic excitations, as phonon excitations would typically increase with  $Q^2$ . An analysis of the  $18 \text{ K}$  spectra revealed that within experimental error the  $Q$  dependence is the same for the transitions **I**–**IV** for all three compounds.

Alternating current (AC) magnetic susceptibility data were collected for  $[\text{Mn}_4\text{O}_3\text{Br}(\text{OAc})_3(\text{dbm})_3]$  in the  $1.87$ – $3.8 \text{ K}$  range with zero DC field and a  $1.0 \text{ G}$  oscillating field. The experimental data for oscillating frequencies of  $250$ ,  $499$ , or  $997 \text{ Hz}$  are shown in Figure 7 as full squares, triangles, and circles, respectively. The in-phase AC magnetic susceptibility data shown in the upper part of Figure 7 gradually decrease from a plateau of  $11.68 \text{ emu K mol}^{-1}$  between  $3.8$  and  $3.4 \text{ K}$  to  $8.67$ ,  $6.53$ , and  $4.49 \text{ emu K mol}^{-1}$  at  $T = 1.87 \text{ K}$  for oscillating

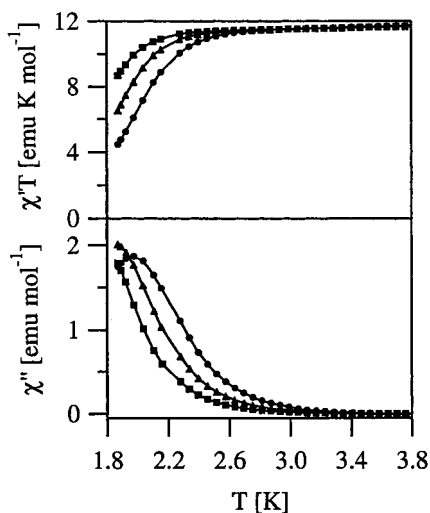


**Figure 7.** AC magnetic susceptibility data for  $[Mn_4O_3Br(OAc)_3(dbm)_3]$ . The upper and lower part depict the in-phase ( $\chi' T$ ) and out-of-phase ( $\chi''$ ) data for oscillating frequencies of 250 Hz (full squares), 499 Hz (full triangles), and 997 Hz (full circles), respectively. The lines in the lower part are drawn to guide the eyes.

**Table 2.** Comparison of the Exchange Parameters  $J_1$  and  $J_2$  and the First Excited Spin Level in  $[Mn_4O_3X(OAc)_3(dbm)_3]$  ( $X = Br, Cl, OAc$ , and  $F$ )<sup>15,16</sup>

label	$J_1$ [cm <sup>-1</sup> ]	$J_2$ [cm <sup>-1</sup> ]	$E( 5\frac{7}{2}\rangle)$ [cm <sup>-1</sup> ]	$\alpha$ [deg]
Cl	-28.4	8.3	184.8	45.1
Br	-30.1	7.4	179.1	42.5
OAc	-33.9	5.4	166.5	53.5
F	-20.8	7.4	151.2	54.2

<sup>a</sup>  $\alpha$  is the mean angle between the JT elongated axes of the single ions and the pseudo- $C_3$  axis of the molecule.<sup>15,16</sup>

frequencies of 250, 499, or 997 Hz, respectively. The decrease of  $\chi' T$  is concomitant with the onset of an out-of-phase AC signal  $\chi''$  depicted in the lower part of Figure 7. These frequency dependent out-of-phase signals  $\chi''$  are a clear sign of the onset of a slowing down of the magnetic relaxation. The maxima of the out-of-phase data  $\chi''$  as a function of temperature for the three oscillating frequencies are collected in Table 4.

## Analysis and Discussion

**Structure and Exchange Coupling in the  $Mn(III,IV)_4O_3X$  Cube.** The compounds  $[Mn_4O_3X(OAc)_3(dbm)_3] \cdot nCH_2Cl_2$  with  $X = Br, Cl$ , and  $OAc$  crystallize in the monoclinic space group  $P2_1/n$  and with  $X = F$  in the triclinic space group  $P\bar{1}$ . The structure of the  $[Mn_4O_3X(OAc)_3(dbm)_3]$  unit is shown in Figure 1a. The cluster possesses a  $[Mn_4(\mu_3-O)_3(\mu_3-X)]^{6+}$  distorted cubane core with a  $Mn(III)_3-Mn(IV)$  trapped-valence oxidation state description. Geometrically the  $[Mn_4(\mu_3-O)_3(\mu_3-X)]^{6+}$  core consists of a trigonal Mn<sub>4</sub> pyramid with the Mn(IV) ion at the apex, a  $\mu_3-X^-$  ion bridging the basal plane, and a  $\mu_3-O^{2-}$  ion bridging each of the remaining three faces. The distorted octahedral ligation of each metal ion is completed by bridging acetate (Mn(III) and Mn(IV)) and terminal dibenzoylmethane (dbm) (Mn(III)) ligands. The crystallographic point symmetry of the clusters is  $C_1$ ; it can be approximated by  $C_{3v}$  with a pseudo- $C_3$  axis passing through the Mn(IV) and  $X^-$  ions. The three Mn(III) octahedra are Jahn-Teller (JT) distorted, and the elongated JT axes fall along the  $X-Mn(III)-O$  (acetate) directions. The mean angle  $\alpha$  between the pseudo- $C_3$  axis and these JT axes is listed in Table 2 for  $X = Br, Cl, OAc$ , and  $F$ .<sup>15,16</sup>

The exchange coupling in the  $Mn(III,IV)_4O_3X$  cube has been studied in detail by magnetic susceptibility measurements.<sup>15,16</sup> Assuming  $C_{3v}$  symmetry for the cluster and isotropic exchange interactions the appropriate spin Hamiltonian is given by:

$$\hat{H}_{ex} = -2J_1(\hat{S}_1\hat{S}_4 + \hat{S}_2\hat{S}_4 + \hat{S}_3\hat{S}_4) - 2J_2(\hat{S}_1\hat{S}_2 + \hat{S}_1\hat{S}_3 + \hat{S}_2\hat{S}_3) \quad (1)$$

with  $S_1 = S_2 = S_3 = 2$  for the Mn(III) ions and  $S_4 = \frac{3}{2}$  for the Mn(IV) ion, respectively.  $J_1$  and  $J_2$  are the Mn(III)-Mn(IV) and Mn(III)-Mn(III) exchange coupling constants, respectively, and are schematically depicted in Figure 1b. By using the equivalent operator approach based on the Kambe vector coupling method the following expression for the energies  $E(S_T)$  is derived:

$$E(S_T) = -J_1[S_T(S_T + 1) - S_A(S_A + 1)] - J_2[S_A(S_A + 1)] \quad (2)$$

with  $\vec{S}_A = \vec{S}_1 + \vec{S}_2 + \vec{S}_3$  and  $\vec{S}_T = \vec{S}_A + \vec{S}_4$ , respectively. In Table 2 the experimentally determined exchange parameters  $J_1$  and  $J_2$  for  $[Mn_4O_3X(OAc)_3(dbm)_3]$  ( $X = Br, Cl, OAc$ , and  $F$ ) are summarized.<sup>15,16</sup> In all compounds the dominant antiferromagnetic Mn(III)-Mn(IV) exchange interaction  $J_1$  leads to a  $|S_AS_T\rangle = |6\frac{9}{2}\rangle$  cluster-ground state. Superexchange pathways involving the oxide bridges appear to control the Mn(III)-Mn(IV) ( $J_1$ ) and Mn(III)-Mn(III) ( $J_2$ ) exchange interactions, as the superexchange pathway along the  $X^-$  involves a JT elongated bond and is thus less efficient.<sup>15,16</sup>

In the fourth column of Table 2 we list the position of the first excited cluster-spin state  $|5\frac{7}{2}\rangle$  calculated from the experimental  $J_1$  and  $J_2$  values. Its energy decreases in the series  $X = Cl, Br, OAc$ , and  $F$  from 184.8 cm<sup>-1</sup> to 151.2 cm<sup>-1</sup>. These excited states can be neglected in the analysis of our INS data, which cover the energy range 0–5.25 cm<sup>-1</sup>. We conclude that the observed INS excitations correspond to transitions within the energetically split  $|S_AS_T\rangle = |6\frac{9}{2}\rangle$  cluster-ground state.

**Zero-Field Splitting in the  $|6\frac{9}{2}\rangle$  Cluster-Ground State.** The Jahn-Teller effect tetragonally elongates the octahedral coordination of the Mn(III) ions along the  $X-Mn(III)-O$  direction, thus the ground state is  $^5B_1$  in the approximate  $C_{4v}$  and  $^5A$  in the actual  $C_1$  single-ion symmetry. The degeneracy of this state is further removed by second-order spin-orbit coupling with excited states in zero magnetic field. The resulting zero-field splitting (ZFS) for each Mn(III) ion will give rise to a ZFS of the cluster states. The local principal anisotropy axis at each Mn(III) ion lies along the JT elongation axis, whereas the principal anisotropy tensor of the cluster lies along the pseudo- $C_3$  axis. Thus, the axial ZFS parameter of the  $|6\frac{9}{2}\rangle$  cluster-ground state is given by:<sup>25</sup>

$$D_{\text{cluster}} = D_{|6\frac{9}{2}\rangle} = \frac{105}{242} D_{\text{Mn(III)}} \cos^2(\alpha) \quad (3)$$

where  $D_{\text{Mn(III)}}$  is the axial single-ion ZFS and  $\alpha$  the mean angle between the JT elongated axis of the single ion and the pseudo- $C_3$  axis of the cluster.

The symmetry of the single-ion coordination is only approximately  $C_{4v}$  and the cluster symmetry is only approximately  $C_{3v}$ . The appropriate spin Hamiltonian for the ZFS in the  $|6\frac{9}{2}\rangle$  cluster-ground state in the true  $C_1$  symmetry is thus:

$$\hat{H}_{\text{ZFS}} = D_{\text{cluster}}[\hat{S}_z^2 - \frac{1}{3}S(S+1)] + E_{\text{cluster}}(\hat{S}_x^2 - \hat{S}_y^2) + B_4^0 \hat{O}_4^0 \quad (4)$$

where  $\hat{O}_4^0 = 35\hat{S}_z^4 - 30S(S+1)\hat{S}_z^2 + 25\hat{S}_z^2 + 6S(S+1)$ .

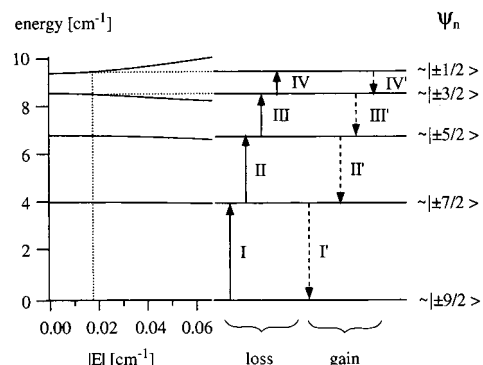


**Figure 8.** Left: Energy sublevels of the  $S = \frac{9}{2}$  cluster ground state as a function of the rhombic ZFS parameter  $|E|$ , calculated for  $D = -0.469 \text{ cm}^{-1}$  and  $B_4^0 = -7.9 \times 10^{-5} \text{ cm}^{-1}$  using eq 4. The dotted lines indicate the best fit to the experimental data for  $[\text{Mn}_4\text{O}_3\text{OAc}(\text{OAc})_3(\text{dbm})_3]$ . Right: Experimentally determined ground-state splitting of  $[\text{Mn}_4\text{O}_3\text{OAc}(\text{OAc})_3(\text{dbm})_3]$ . The full and dashed arrows correspond to the observed neutron-energy loss and gain transitions, respectively. The labeling of the transitions is the same as in Figure 2.

The first axial term in eq 4 is expected to dominate the second rhombic term. The third quartic term in eq 4 was introduced to interpret high-field high-frequency EPR experiments of the  $[\text{Mn}_4\text{O}_3\text{Cl}(\text{OAc})_3(\text{dbm})_3]$  cluster.<sup>17</sup> No rhombic term was taken into account in ref 17, and the parameters  $D_{\text{cluster}}$  and  $B_4^0$  were determined as  $-0.53$  and  $-7.3 \times 10^{-5} \text{ cm}^{-1}$ , respectively.

The spin Hamiltonian in eq 4 does not commute with  $\hat{S}^2$ , and thus the  $|6\frac{9}{2}\rangle$  cluster-ground state will split. Neglecting the rhombic term, eq 4 still commutes with  $\hat{S}_z$ , and the split components of the ground state are characterized by  $|S_T \pm M\rangle$ , abbreviated  $|\pm M\rangle$  in the following.  $M$  is the projection of the total spin  $S_T$  on the pseudo- $C_3$  axis of the cluster. The rhombic term  $E(\hat{S}_x^2 - \hat{S}_y^2)$  in eq 4 does not commute with  $\hat{S}_z$  and will thus lead to a mixing of the basis functions with  $\Delta M = \pm 2$ . The proper cluster wave functions in the presence of a rhombic anisotropy will thus have the form

$$\psi_n = \sum_M a_n(M) |S_T M\rangle \quad (5)$$

where  $a_n(M)$  are the eigenvector coefficients obtained by diagonalizing the energy matrix of the operator in eq 4. However, since the axial term is the leading term, this mixing will be small, and the cluster wave functions are still characterized by a leading  $|\pm M\rangle$  term. Equation 4 will in the following be used to analyze the INS data with  $D$ ,  $|E|$ , and  $B_4^0$  as adjustable parameters.

In a first empirical step we derive the energy splitting of the ground state from the temperature-dependent data, such as shown in Figure 2 for  $X = \text{OAc}$ . The dominant peak **I** in the 1.8 K INS spectrum on the neutron-energy loss side corresponds to a transition between the lowest-energy ZFS levels. With increasing temperature higher levels are thermally populated leading to the observation of bands **II**, **III**, and **IV** in energy loss and **I'-IV'** in energy gain. The hot bands are observed at progressively lower energies, and the 18 K spectra in Figure 4 exhibit quite a regular picket-fence pattern. The resulting empirical energy level scheme thus obtained for the four title clusters is schematically shown in Figure 8, and the energy intervals for all the four compounds are listed in Table 1. The validity of this splitting pattern is very nicely confirmed by comparing the observed temperature dependence of the INS intensities with that calculated from the Boltzmann populations

of the cluster levels in Table 1. This is shown in Figure 3, and the agreement is gratifying.

In the next step we compare the experimental zero-field splittings with the calculated ones using eq 4. The experimental energy patterns are approximately of the Landé type, which immediately tells us that the axial ZFS term in eq 4 is the leading term. And from the fact that the energy intervals are getting smaller with increasing energy it follows that  $D$  has a negative value.

For  $X = \text{OAc}$  the actual energy intervals have ratios of  $4.00:2.75:1.71:0.93$ . The deviation from the Landé type splitting pattern of  $4:3:2:1$  is significant, and the second and third term in eq 4 are obviously significant. We performed calculations with  $B_4^0 \neq 0$  and  $|E| = 0$  as well as  $B_4^0 \neq 0$  and  $|E| \neq 0$ . The results are collected in Table 3. Both parameters lead to significant improvement of the purely axial model with only the  $D$  parameter, and both  $B_4^0$  and  $|E|$  are essential.

The importance of the rhombic term in eq 4 can be nicely seen by inspection of Table 3. The model with  $D = -0.469 \text{ cm}^{-1}$  and  $B_4^0 = -7.9 \times 10^{-5} \text{ cm}^{-1}$  provides a fair reproduction of the experimental splitting for  $X = \text{OAc}$ , but the transition **IV** is calculated too low. Inclusion of the rhombic term in the least-squares fit to the experimental data improves the goodness of the fit by a factor of 35, see Table 3. This improvement is significant, and we conclude that the rhombic term is important. The effect of the rhombic term on the energy splittings is illustrated in Figure 8. The energy of the transition **IV** increases with increasing  $|E|$ , thus improving the overall fit of the experimental data, see Table 3. The effect of the rhombic term on the wave functions is shown in Table 5, where the wave functions corresponding to the best fit are collected for all the three compounds  $X = \text{Cl}, \text{Br}$ , and  $\text{OAc}$ . The strongest effect of the rhombic term in eq 4 is on the  $|\pm \frac{3}{2}\rangle$  and  $|\pm \frac{1}{2}\rangle$  levels. The  $E(\hat{S}_x^2 - \hat{S}_y^2)$  term in the Hamiltonian leads to a mixing of these levels, which are only separated by  $-2D + 1260B_4^0$ . As a consequence they repel each other and the cluster wave functions are mixtures of  $|\pm \frac{3}{2}\rangle$  and  $|\pm \frac{1}{2}\rangle$ .

The spin Hamiltonian parameter values leading to the best fits for all the compounds are listed in Table 4. For  $X = \text{F}$  the data do not allow the determination of  $|E|$ . The numbers for the fluoride in Table 4 correspond to the cluster with the highest peak in the convoluted INS bands, see Figure 5.

The axial ZFS parameter  $D$  determined for the four title compounds from variable-field magnetization data were, assuming a negative  $D$ ,  $-0.35$ ,  $-0.35$ ,  $-0.32$ , and  $-0.29 \text{ cm}^{-1}$  for  $X = \text{Cl}, \text{Br}, \text{OAc}$ , and  $\text{F}$ , respectively.<sup>6,15</sup> These values are significantly smaller than the  $D$  values in Table 4. We ascribe this discrepancy to the fact that the fits of the magnetization data in refs 6 and 15 did not consider a full powder average of the magnetization data. Recent full powder average fits of the magnetization data for  $X = \text{Br}$  and  $\text{OAc}$  gave  $D$  values of  $-0.50$  and  $-0.47 \text{ cm}^{-1}$ , respectively,<sup>26</sup> in very good agreement with the values obtained from INS in Table 4. For  $X = \text{Cl}$  the  $D$  value determined from the high-field high-frequency study was  $-0.53 \text{ cm}^{-1}$ , in perfect agreement with our value of  $-0.529 \text{ cm}^{-1}$  obtained by INS. This illustrates the power of spectroscopic techniques in the determination of such ground-state splittings. Our INS data allow a most accurate determination of the transition energies and thus an accurate determination of the spin Hamiltonian parameters.

(26) Wang, S.; Wemple, M. S.; Yoo, J.; Folting, K.; Huffman, J. C.; Hagen, K. S.; Hendrickson, D. N.; Christou, G. *Inorg. Chem.* **2000**, *39*, 1501–1513.

**Table 3.** Experimental and Calculated Transition Energies and Relative Intensities of Transitions **I–IV** Using Eqs 4 and 7 and the Tabulated Parameters  $D$ ,  $|E|$ , and  $B_4^0$  for  $[Mn_4O_3OAc(OAc)_3(dbm)_3]^a$ 

label	energy [cm <sup>-1</sup> ]			intensities [arb. units]			
	exp	calc	calc	calc	exp	calc	calc
$D$ [cm <sup>-1</sup> ]		-0.469	-0.469	-0.469		-0.469	-0.469
$ E $ [cm <sup>-1</sup> ]	-	-	0.017		-	-	0.017
$B_4^0$ [cm <sup>-1</sup> ]	-	$-7.9 \times 10^{-5}$	$-7.9 \times 10^{-5}$		-	$-7.9 \times 10^{-5}$	$-7.9 \times 10^{-5}$
I	4.013(4)	3.744	4.015	4.011	1.00(3)	1.0000	1.0000
II	2.762(5)	2.808	2.779	2.772	1.74(5)	1.7778	1.7778
III	1.714(5)	1.872	1.742	1.713	2.24(5)	2.3333	2.3333
IV	0.937(5)	0.936	0.838	0.937	2.36(6)	2.6667	2.6667
$\chi^2$ [10 <sup>-5</sup> ]	333	111		3.1			

<sup>a</sup> The intensities were scaled to one for transition I.

**Table 4.** Experimentally Determined Cluster and Single-Ion Spin Hamiltonian Parameters for  $[Mn_4O_3X(OAc)_3(dbm)_3]$  (X = Br, Cl, OAc, and F) with Goodness of the Least-squares Fitting Analysis  $\chi^2$ <sup>a</sup>

X	$D$ [cm <sup>-1</sup> ] cluster	$ E $ [cm <sup>-1</sup> ] cluster	$B_4^0$ [10 <sup>-5</sup> cm <sup>-1</sup> ] cluster	$\Delta$ [cm <sup>-1</sup> ]	$D_{Mn(III)}$ [cm <sup>-1</sup> ] single ion	$\chi^2$ [10 <sup>-5</sup> ]	$T_{\max}[\chi'']$ [K]		
	cluster	cluster	cluster	cluster	single ion	[10 <sup>-5</sup> ]	250 Hz	499 Hz	997 Hz
Cl	-0.529	0.022	-6.5	10.66	-2.445	1.0	<1.73	1.80	1.90
Br	-0.502	0.017	-5.1	10.10	-2.130	2.8	<1.76	1.76	1.96
OAc	-0.469	0.017	-7.9	9.43	-3.053	3.1	<1.72	<1.72	1.80
F	-0.379	-	-11.1	7.59	-2.556	3.2	<1.72	<1.72	<1.72

<sup>a</sup> The total calculated energy splitting  $\Delta$  is also given. The temperatures with maximal out-of-phase AC susceptibility signal  $T_{\max}[\chi'']$  as a function of AC frequency in Hz are given for comparison. The data for X = Cl, OAc, and F were taken from ref 6.

There is a steady decrease in the absolute value of  $D$  along the series Cl, Br, OAc, F. It is smaller in the fluoride than in the chloride by 25%. Using eq 3 and the  $\alpha$  values in Table 2 we can derive the axial ZFS parameters for the single ion  $D_{Mn(III)}$ , which are included in the fifth column of Table 4. The range of  $D$  values,  $-2.55 \pm 0.42$  cm<sup>-1</sup> lies well within the range of  $D$  values found in polycrystalline samples of five-coordinate Schiff-base Mn(III) complexes ( $D$  range: -1.0 to -3.8 cm<sup>-1</sup>) and Mn(III) porphyrin complexes ( $D$  range: -1.0 to -3.0 cm<sup>-1</sup>).<sup>27,28</sup> The variation of axial single-ion ZFS parameters  $D_{Mn(III)}$  along the halide series F, Cl, Br may be rationalized in terms of a reduction of the spin-orbit coupling constants of the Mn(III) ions due to increasing covalency.

The quartic ZFS term in eq 4 has been taken into account in the high-field high-frequency EPR study for X = Cl. The derived  $B_4^0$  value  $-7.3 \times 10^{-5}$  cm<sup>-1</sup> nicely agrees within experimental accuracy with our value of  $-6.5 \times 10^{-5}$  cm<sup>-1</sup> derived by INS. There is no clear trend in the  $B_4^0$  values of Table 4 along the series X = Cl, Br, OAc, and F. The rhombic ZFS parameter  $|E|$  is of the order of 3–4% of  $|D|$ . Its sign cannot be determined. In earlier interpretations of magnetic and EPR data the rhombic term was neglected. Our results clearly show the significance of this term. A final remark concerns the inclusion of the rhombic term in the ZFS analysis. As this term mainly affects the energy interval IV we do not see a significant change in the axial and quartic parameters  $D$  and  $B_4^0$ , respectively. The latter two are mainly determined by the energy intervals I, II, and III. This is confirmed by the mentioned nice agreement with the high-field high-frequency EPR study on X = Cl.

**INS Intensities and Wave Functions.** The relative INS intensities, corrected for the corresponding Boltzmann factors, are listed in Table 3 for  $[Mn_4O_3OAc(OAc)_3(dbm)_3]$ . They contain information about the cluster wave functions. Theoretically the intensity of an INS transition  $|\psi_n\rangle \rightarrow |\psi_m\rangle$ , corrected

for the Boltzmann population, is given by the differential magnetic cross-section as follows:<sup>29</sup>

$$\frac{d^2\sigma}{dQdE} = \frac{N}{4} \left\{ \frac{\gamma e^2}{m_e c^2} \right\} \frac{k'}{k} \exp(-2W(Q,T)) \sum_{\alpha,\beta} \left\{ \delta_{\alpha\beta} - \frac{Q_\alpha Q_\beta}{Q^2} \right\} \times \sum_{ij} \{g_i F_i(Q)\} \{g_j F_j(Q)\} \exp(i\vec{Q}(\vec{R}_i - \vec{R}_j)) \langle \psi_n | \hat{S}_i^\alpha | \psi_m \rangle \times \langle \psi_m | \hat{S}_j^\beta | \psi_n \rangle \delta(\hbar\omega + E_n - E_m) \quad (6)$$

In eq 6  $k$  and  $k'$  are the wavenumbers of the incoming and scattered neutrons,  $\vec{Q}$  is the scattering vector,  $\exp(-2W(Q,T))$  is the Debye-Waller factor,  $\hbar\omega$  is the neutron energy,  $\psi_i$  are the cluster wave functions with energies  $E_i$ ,  $g_i$  is the g factor and  $F_i(Q)$  is the magnetic form factor,  $\vec{R}_i$  is the space vector of the  $i$ th Mn ion in the cluster and  $\alpha$  and  $\beta$  stand for the spatial coordinates  $x$ ,  $y$ , and  $z$ ,  $e$  and  $m_e$  are the charge and the mass of the electron, respectively,  $c$  is the speed of light, and  $\gamma = -1.91$  is the gyromagnetic constant of the neutron.

In the calculation of the relative INS intensities we make use of the fact that all transitions exhibit the same  $Q$  dependence. We can thus evaluate the cross-section in eq 6 at  $Q = 0 \text{ \AA}^{-1}$  where  $F_i(Q)$  are equal to unity. For the relative intensities we are thus left with the calculation of the squares of the transition moments:<sup>30</sup>

$$|\langle \psi_n | \hat{S}_\perp | \psi_m \rangle|^2 = \frac{1}{3} (2|\langle \psi_n | \hat{S}_z | \psi_m \rangle|^2 + |\langle \psi_n | \hat{S}^+ | \psi_m \rangle|^2 + |\langle \psi_n | \hat{S}^- | \psi_m \rangle|^2) \quad (7)$$

where  $\hat{S}_\perp$  is the spin component perpendicular to the scattering vector  $\vec{Q}$  and  $S^+$  and  $S^-$  are the angular momentum raising and lowering operators, respectively. By using the eigenfunctions (Table 5) obtained by diagonalizing the ZFS Hamiltonian in eq 4 with the parameters for  $[Mn_4O_3OAc(OAc)_3(dbm)_3]$  in Table 4 we get the calculated relative intensities in Table 3.

(27) Kennedy, B. J.; Murray, K. S. *Inorg. Chem.* **1985**, 24, 1552.  
(28) Dugard, L. B.; Behere, D. V.; Marathe, V. R.; Mitra, S. *Chem. Phys. Lett.* **1984**, 104, 353.

(29) Marshall, W.; Lovesey, S. W. *Theory of Thermal Neutron Scattering*; Clarendon Press: Oxford, 1971.

(30) Birgenau, R. J. *J. Phys. Chem. Solids* **1972**, 33, 59.

**Table 5.** Calculated Energies with Corresponding Wavefunctions by Diagonalizing the Spin Hamiltonian in Eq 4 with the Parameters in Table 4 for  $[\text{Mn}_4\text{O}_3\text{X}(\text{OAc})_3(\text{dbm})_3]$  ( $\text{X} = \text{Br}$ ,  $\text{Cl}$ , and  $\text{OAc}$ )<sup>a</sup>

energy [cm <sup>-1</sup> ]	wavefunctions
$\text{X} = \text{Cl}$	
0.0000	$+0.9998 \pm\frac{9}{2}\rangle+0.0176 \pm\frac{5}{2}\rangle$
4.4409	$+0.9992 \pm\frac{7}{2}\rangle+0.0395 \pm\frac{3}{2}\rangle+0.0018 \mp\frac{1}{2}\rangle$
7.5748	$+0.0175 \mp\frac{9}{2}\rangle-0.9963 \mp\frac{5}{2}\rangle-0.0112 \pm\frac{3}{2}\rangle-0.0838 \mp\frac{1}{2}\rangle$
9.5379	$-0.0387 \pm\frac{7}{2}\rangle-0.0316 \mp\frac{5}{2}\rangle+0.9679 \pm\frac{3}{2}\rangle+0.2463 \mp\frac{1}{2}\rangle$
10.6645	$+0.0081 \pm\frac{7}{2}\rangle-0.0784 \mp\frac{5}{2}\rangle-0.2479 \pm\frac{3}{2}\rangle+0.9656 \mp\frac{1}{2}\rangle$
$\text{X} = \text{Br}$	
0.0000	$+0.9999 \pm\frac{9}{2}\rangle+0.0140 \pm\frac{5}{2}\rangle$
4.1844	$+0.9995 \pm\frac{7}{2}\rangle+0.0313 \pm\frac{3}{2}\rangle+0.0011 \mp\frac{1}{2}\rangle$
7.1705	$+0.0140 \mp\frac{9}{2}\rangle-0.9977 \mp\frac{5}{2}\rangle-0.0007 \pm\frac{3}{2}\rangle-0.0658 \mp\frac{1}{2}\rangle$
9.0681	$-0.0308 \pm\frac{7}{2}\rangle-0.0201 \mp\frac{5}{2}\rangle+0.9788 \pm\frac{3}{2}\rangle+0.2017 \mp\frac{1}{2}\rangle$
10.1011	$+0.0053 \pm\frac{7}{2}\rangle-0.0630 \mp\frac{5}{2}\rangle-0.2025 \pm\frac{3}{2}\rangle+0.9772 \mp\frac{1}{2}\rangle$
$\text{X} = \text{OAc}$	
0.0000	$+0.9999 \pm\frac{9}{2}\rangle+0.0146 \pm\frac{5}{2}\rangle$
4.0111	$+0.9994 \pm\frac{7}{2}\rangle+0.0335 \pm\frac{3}{2}\rangle+0.0013 \mp\frac{1}{2}\rangle$
6.7828	$+0.0146 \mp\frac{9}{2}\rangle-0.9973 \mp\frac{5}{2}\rangle-0.0082 \pm\frac{3}{2}\rangle-0.0719 \mp\frac{1}{2}\rangle$
8.4960	$-0.0329 \pm\frac{7}{2}\rangle-0.0239 \mp\frac{5}{2}\rangle+0.9748 \pm\frac{3}{2}\rangle+0.2193 \mp\frac{1}{2}\rangle$
9.4327	$+0.0062 \pm\frac{7}{2}\rangle-0.0683 \mp\frac{5}{2}\rangle-0.2204 \pm\frac{3}{2}\rangle+0.9730 \mp\frac{1}{2}\rangle$

<sup>a</sup> Only basis functions with coefficients  $a_n(M) > 0.0010$  (eq 5) are listed.

The agreement within the experimental accuracy is perfect. For comparison Table 3 also shows the relative intensities calculated with an axial and an axial-quartic model, that is, neglecting the quartic/rhombic and rhombic terms in eq 4, respectively. As the axial and quartic ZFS terms are diagonal in the  $|\pm M\rangle$  basis set they both have the same effect on the relative intensities. The calculated relative intensity ratios of **I:II:III:IV** without the rhombic term are 9:16:21:24. The agreement with the experimental ratios is significantly worse than with inclusion of the rhombic term, see Table 3. The calculated relative intensities of transitions **III** and **IV** are calculated too high in the purely axial model. This is another direct proof of the importance of the rhombic term in eq 4. It also demonstrates the important information contained in the INS intensities. For the calculation of the Q-dependence of the INS intensities of transitions **I** we need to take the spin coupling of the Mn(III) and Mn(IV) ions in the  $\text{Mn}(\text{III},\text{IV})_4\text{O}_3\text{X}$  cube into account. We thus have to solve the full spin Hamiltonian including the exchange coupling and the ZFS:

$$\hat{H}_{\text{tot}} = \hat{H}_{\text{ex}} + \hat{H}_{\text{ZFS}} = -2J_1(\hat{S}_1\hat{S}_4 + \hat{S}_2\hat{S}_4 + \hat{S}_3\hat{S}_4) - 2J_2(\hat{S}_1\hat{S}_2 + \hat{S}_1\hat{S}_3 + \hat{S}_2\hat{S}_3) + D[\hat{S}_z^2 - \frac{1}{3}S(S+1)] + E(\hat{S}_x^2 - \hat{S}_y^2) + B_4^0\hat{O}_4^0 \quad (8)$$

This spin Hamiltonian is not diagonal in the spin quantum numbers  $S_A$ ,  $S_T$ , and  $M$ , and thus the eigenfunctions will be given

by appropriate linear combinations of the basis functions  $|S_AS_TM\rangle$  by:

$$\psi_n = \sum_{S_A, S_T, M} a_n(S_A, S_T, M) |S_AS_TM\rangle \quad (9)$$

where  $a_n(S_A, S_T, M)$  are the eigenvector coefficients of the cluster levels.

These wave functions and eq 6 are used for the calculation of the  $Q$  dependence of the INS intensities. The matrix elements of  $\hat{S}_i^\alpha$  and  $\hat{S}_j^\beta$  are best evaluated by using irreducible tensor operators techniques.<sup>31</sup> Since our experiments are performed on a powdered sample with random orientation of the tetramer with respect to  $Q$ , the cross section has to be averaged in  $Q$  space. For the evaluation of eq 6 we made use of a numerical algorithm developed in ref 32 which is of general validity. The form factors  $F_i(Q)$  and the Mn–Mn distances  $R_{ij}$  in the relevant calculation are taken from the literature.<sup>15,16,33</sup> The mean Mn–Mn distance increases from 2.97, 3.00, 3.03, to 3.04 Å along the series  $\text{X} = \text{F}$ ,  $\text{OAc}$ ,  $\text{Cl}$ , and  $\text{Br}$ . Due to the same spin coupling in the cluster-ground state and the similar mean Mn–Mn distances we calculate essentially the same  $Q$  dependencies of the scattering intensities for  $\text{X} = \text{OAc}$ ,  $\text{Cl}$ , and  $\text{Br}$ . This is in good agreement with the observation that all three compounds exhibit essentially the same experimental  $Q$  dependence, see Figure 6. The experimental variation of the intensities with  $Q$  in the range 0.2–2.3 Å<sup>-1</sup> is very small. The calculated  $Q$  dependence for  $\text{X} = \text{Br}$  is shown as a dotted line in Figure 6. It is also relatively flat, but clearly shows more variation than the experimental data. Since the high quality of our wave functions has been proven in the analysis of the relative intensities, we have to ascribe this discrepancy in the  $Q$  dependence to another cause. We attribute it to multiple scattering processes in our sample. A fraction of these processes are incoherent as a result of the hydrogen atoms present in the sample. The  $k$  vectors of both incoming and scattered neutrons are thus no longer well defined, and as a result the  $Q$  vector is no longer well defined. This leads to an averaging of the scattered intensity as a function of  $Q$ . The solid line in Figure 6 represents a calculation in which  $Q$  is assumed to cover the range  $Q \pm 0.5$  Å<sup>-1</sup>. It does bring the calculation in line with experiment as expected. We have observed a loss of sharpness of the definition of  $Q$  in other INS experiments using undeuterated samples.

**Relevance of the Rhombic ZFS for the Magnetization Relaxation Behavior.** Table 4 lists the temperatures  $T_{\text{max}}$  of the maximal out-of-phase signal  $\chi''$  in an alternating current (AC) susceptibility measurement as a function of the frequency of the alternating field. The data for  $[\text{Mn}_4\text{O}_3\text{X}(\text{OAc})_3(\text{dbm})_3]$  ( $\text{X} = \text{Cl}$ ,  $\text{OAc}$ , and  $\text{F}$ ) are taken from the literature.<sup>6</sup> For  $[\text{Mn}_4\text{O}_3\text{Br}(\text{OAc})_3(\text{dbm})_3]$  the data were extracted from the out-of-phase AC susceptibility data in the lower part of Figure 7.

These frequency dependent  $T_{\text{max}}[\chi'']$  indicate the onset of a slowing down of the magnetization relaxation, which is taken as a fingerprint that the individual molecules are acting as single-domain magnetic units. At the tabulated temperatures  $T_{\text{max}}[\chi'']$

(31) Silver, B. L. *Irreducible Tensor Operators*; Academic Press: New York, 1976.

(32) Borrás-Almenar, J. J.; Clemente-Juan, J. M.; Coronado, E.; Tsukerblat, B. S. *Inorg. Chem.* 1999, 38, 6081–6088.

(33) Watson, R. E.; Freeman, A. J. *Acta Crystallogr.* 1961, 27.

(34) Andres, H.; Aebersold, M.; Güdel, H. U.; Clemente-Juan, J. M.; Coronado, E.; Büttner, H.; Kearly, G.; Zolliker, M. *Chem. Phys. Lett.* 1998, 289, 224.

(35) Andres, H.; Clemente-Juan, J. M.; Aebersold, M.; Güdel, H. U.; Coronado, E.; Büttner, H.; Kearly, G.; Melero, J.; Burriel, R. *J. Am. Chem. Soc.* 1999, 121, 10028–10034.

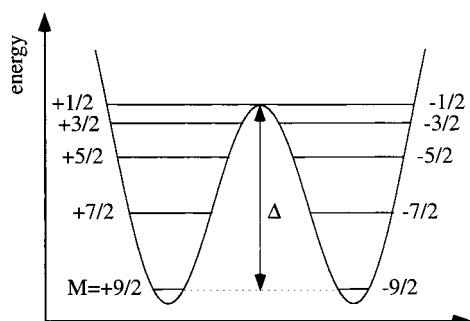


**Figure 9.** Plot of the potential-energy double well for  $[Mn_4O_3Cl(OAc)_3(dbm)_3]$  with the parameters  $D = -0.529 \text{ cm}^{-1}$ ,  $|E| = 0.022 \text{ cm}^{-1}$  and  $B_4^0 = -6.5 \times 10^{-5} \text{ cm}^{-1}$ . The potential energy barrier is denoted as  $\Delta$ .

in Table 4 the frequency of the alternating field equals the rate at which the magnetic moments flip their spins. This can be rationalized with the schematic Figure 9. It shows the ZFS levels with positive  $M$  values on the left, separated by an energy barrier of height  $\Delta$  from the corresponding levels with negative  $M$  on the right. A transition  $M \rightarrow -M$  can occur either thermally by overcoming the energy barrier or by quantum tunneling. Below a critical temperature  $T_B$ , the blocking temperature, the magnetization relaxation gets so slow that on our laboratory time scale it seems blocked. Thus, below  $T_B$  the single molecules are magnetizable and can store a bit of information.

In the temperature regime above  $T_B$  a two-phonon Orbach spin-lattice process dominates the relaxation behavior. It is a thermally activated process, and thus the relaxation rate  $\tau$  is given by:

$$\tau = \tau_0 \exp\left(\frac{\Delta}{k_B T}\right) \quad (10)$$

where  $k_B$  is the Boltzmann constant. With the ZFS parameters in Table 4 we calculate  $\Delta$  as 7.59, 9.43, 10.10, and  $10.66 \text{ cm}^{-1}$  for  $X = F$ , OAc, Br, and Cl, respectively. By assuming  $\tau_0$  to be the same for the four title compounds a decreasing relaxation rate  $\tau$  is calculated along the series  $X = F$ , OAc, Br, and Cl. In an AC susceptibility measurement at a given frequency of the alternating field we thus expect an increase of  $T_{\max}[\chi'']$  along this series  $X = F$ , OAc, Br, and Cl. Apart from the relative order of  $X = Cl$  and Br this is nicely borne out by the experimental trend in  $T_{\max}[\chi'']$  in Table 4. The interchanged order of Cl and Br results from the tunneling, as will be shown below.

In the above analysis we have neglected the direct quantum tunneling of the magnetization. This tunneling requires an anisotropy perpendicular to the  $z$ -axis. Aubin and co-workers have postulated that this transverse field is generated by a small internal field of the nuclear spins.<sup>17</sup> Here we clearly show that the dominant transverse field has its origin in the crystal-field anisotropy. It is the rhombic term in eq 4 with the parameters in Table 4. Although the term  $E(\hat{S}_x^2 - \hat{S}_y^2)$  in eq 4 in first order only mixes basis functions with  $\Delta M = \pm 2$  we see a considerable higher order mixing of basis functions; The wave functions obtained from the energy calculation using eq 4 with the best fit parameters in Table 4 are collected for  $X = Cl$ , Br, and OAc in Table 5. The contamination of the  $|\pm M\rangle$  functions is particularly strong for the higher-energy levels, making direct quantum tunneling processes through these particularly probable. Experimentally this direct quantum tunneling of the magnetization effectively leads to a reduction of the potential barrier  $\Delta$ . For  $[Mn_4O_3Cl(OAc)_3(dbm)_3]$  a barrier height of  $8.21 \text{ cm}^{-1}$  has been determined from magnetization relaxation

measurements.<sup>17</sup> This value is 22% lower than the calculated  $\Delta$ . For  $X = Br$  we roughly estimate an effective barrier height of  $8.30 \text{ cm}^{-1}$  from the  $T_{\max}[\chi'']$  data shown in Figure 2. The value of  $\Delta$  determined by INS is  $10.10 \text{ cm}^{-1}$  (Table 4). The effective reduction is thus 18%, that is, lower than in the chloride. Inspection of the wave functions in Table 5 provides an immediate explanation. As a result of the smaller  $|E|$  parameter (Table 4) the wave functions are significantly less mixed in the bromide than in the chloride. This in turn leads to smaller tunneling rates and thus a higher effective barrier for tunneling in the bromide despite the lower  $\Delta$  value. Thus both the energies and the wave functions derived from INS for the title compounds correlate beautifully with the magnetic quantum tunneling behavior. For  $X = Cl$  a temperature-independent tunneling rate constant of  $3.2 \times 10^{-2} \text{ s}^{-1}$  has been derived from the magnetic measurements below  $T_B$ . The wave functions determined in the present study can conceivably be used to theoretically calculate such tunneling rates.

### Conclusions

The title compounds  $[Mn_4O_3X(OAc)_3(dbm)_3]$  ( $X = Br$ , Cl, OAc, and F) are illustrative examples of single-molecule magnets, exhibiting unusual magnetic behavior such as quantum tunneling of the magnetization at very low temperatures. These physical properties can be influenced by varying the ligand  $X$  in the chemical formula. A high-resolution inelastic neutron scattering (INS) study on these spin clusters has led to a very precise determination of the ZFS of the  $S = 9/2$  cluster-ground state. We unambiguously show the presence of a dominant axial anisotropy with a negative parameter  $D$ , a quartic term with parameter  $B_4^0$  and a small rhombic anisotropy with parameter  $|E|$  in the ZFS. The magnitude of the transverse ZFS parameter  $|E|$  directly follows from the experimentally determined energy-level diagrams as well as the relative intensities of the magnetic INS transitions. This term has not previously been used in the analysis of the magnetization and high-frequency high-field EPR data. It is the key term, however, for an understanding of the quantum tunneling behavior in this series of clusters. It leads to a mixing of the  $|\pm M\rangle$  basis functions which, in turn, determines the tunneling rates.

The presented high-resolution INS study has been performed on completely undeuterated compounds. Until recently, we have assumed that full deuteration is essential for this type of experiment due to the large incoherent neutron cross-section of the hydrogen. Apparently, the density of vibrational states with a substantial hydrogen contribution is very small in the energy-transfer range of  $0-6 \text{ cm}^{-1}$  probed in the present experiments. Two complications did arise from the hydrogen content in our samples; first a temperature dependent shoulder of the elastic peak due to quasi-elastic scattering and second the smeared out Q-dependence of the magnetic INS intensities. More substantial complications due to quasi-elastic scattering have been avoided by choosing a very high incident neutron wavelength of  $7.5 \text{ \AA}^{-1}$ , at which the quasi-elastic intensity is well separated from the magnetic inelastic intensity. The complications due to multiple scattering may be reduced by choosing an optimal shape of the sample container. Despite these possible improvements for future work the overall quality of the INS data is excellent and has enabled a very detailed data analysis and led to a more profound understanding of the quantum tunneling processes in this interesting family of spin clusters.

**Acknowledgment.** This work was financially supported by the Swiss and U.S.A. National Science Foundations.